Vanishing electron g factor and long-lived nuclear spin polarization in weakly strained nanohole-filled GaAs/AlGaAs quantum dots

A. Ulhaq,[1] Q. Duan,[1] E. Zallo,[2,3] F. Ding,[2] O. G. Schmidt,[2] A. I. Tartakovskii,[1] M. S. Skolnick,[1] and E. A. Chekhovich[1,*]

[1]*Department of Physics and Astronomy, University of Sheffield, Sheffield, S3 7RH, United Kingdom*
[2]*Institute for Integrative Nanoscience, IFW Dresden, Helmholtz str. D-01069, Dresden, Germany*
[3]*Paul-Drude-Institut für Festkörperelektronik, Hausvogteiplatz 5-7, 10117 Berlin, Germany*

GaAs/AlGaAs quantum dots grown by *in situ* droplet etching and nanohole in-filling offer a combination of strong charge confinement, optical efficiency, and high spatial symmetry advantageous for polarization entanglement and spin-photon interface. Here, we study experimentally electron and nuclear spin properties of such dots. We find nearly vanishing electron g factors ($g_e < 0.05$), providing a potential route for electrically driven spin control schemes. Optical manipulation of the nuclear spin environment is demonstrated with nuclear spin polarization up to 65% achieved. Nuclear magnetic resonance spectroscopy reveals two distinct types of quantum dots: with tensile and with compressive strain along the growth axis. In both types of dots, the magnitude of strain $\epsilon_b < 0.02\%$ is nearly three orders of magnitude smaller than in self-assembled dots: On the one hand, this provides a route for eliminating a major source of electron spin decoherence arising from nuclear quadrupolar interactions, and on the other hand such strain is sufficient to suppress nuclear spin diffusion leading to a stable nuclear spin bath with nuclear spin lifetimes exceeding 500 s. The spin properties revealed in this work make this new type of quantum dot an attractive alternative to self-assembled dots for the applications in quantum information technologies.

I. INTRODUCTION

Electron or hole spin in semiconductor quantum dots is a prime candidate for applications in quantum information processing [1–6]. Due to the three-dimensional (3D) confinement, it is insensitive to spin-orbit relaxation effects and at the same time is accessible for coherent manipulation and can be interfaced optically. The coherence in this system is mainly limited by hyperfine coupling with the nuclear spin bath [1,6–8]. Single spin qubit manipulation in quantum dots, therefore, demands an auxiliary control over nuclear spin environment. Such control can be realized by maximizing polarization of 10^4–10^5 nuclei in a single quantum dot [9–11], enabling the formation of well-defined nuclear spin states and in effect reducing the influence of the nuclear field fluctuations [12,13]. Furthermore, strain-induced quadrupolar effects have been shown to be a major source of electron spin decoherence [14,15], thus, it is desirable to find a high-quality quantum dot system where nuclear quadrupolar effects are minimized.

Electron or hole spin manipulation in semiconductor quantum dot (QD) system using resonant ultrafast optical pulses [3–5] has been demonstrated, but scalability in such schemes is challenging. An alternative approach is to induce controlled spin rotation by manipulating the coupling to the external magnetic field [16]. This can be achieved by electrical modulation of the g factor. However, such a scheme critically depends on the ability to change the sign of g, thus requiring quantum dots with close-to-zero electron or hole g factor [17,18].

Self-assembled InGaAs/GaAs QDs have been the primary system of choice for spin studies over the last two decades due

to their excellent optical properties, and strong quantum confinement, which can not be achieved in monolayer-fluctuation GaAs/AlGaAs dots. Only recently the potential of droplet epitaxial (DE) grown GaAs QDs has been identified [19–21]. In particular, nanohole-filled droplet epitaxial (NFDE) dots formed by *in situ* etching and nanohole in-filling [22] provide confinement and excellent optical efficiency, while on the other hand exhibiting high symmetry not achievable previously in self-assembled dots [23]. Such unique combination of properties make NFDE dots ideal candidates for polarization entanglement and spin-photon interfaces [24]. This system has already exhibited an efficient interface between rubidium atoms and a quantum dot [25,26]. However, the understanding of the spin properties in such quantum dots is still lacking.

Here, we use optical and nuclear magnetic resonance (NMR) spectroscopy to study the properties of the single charge spins and the nuclear spin environment in NFDE grown GaAs/AlGaAs QDs. Magnetophotoluminescence measurements reveal close-to-zero electron g factors, due to the electron wave-function overlap with the AlGaAs barrier, a prerequisite for electrical spin manipulation. We demonstrate efficient dynamic nuclear polarization (DNP) as large as 65%. By measuring the excitation wavelength dependence, we identify three mechanisms of DNP: (i) via optical excitation of quantum well states, (ii) via resonant optical excitation of the dot ground or excited states, and (iii) via resonant excitation of neighboring dots made possible by interdot charge tunneling.

Radio-frequency (rf) excitation is used to measure NMR spectra revealing the presence of small ($<0.02\%$) residual strain. Surprisingly, we observe two subensembles of QDs: one with compressive and another with tensile strain along the growth axis. This allows us to identify these two types of dots as formed in the nanoholes and at the rims of the nanoholes, respectively. On the one hand, the smallness of strain implies small quadrupolar effects ($\lesssim 20$ kHz) which

*e.chekhovich@sheffield.ac.uk

may greatly increase electron spin coherence [14,15]. On the other hand, we show that such strain is large enough to result in very stable nuclear spin baths with nuclear spin relaxation times >500 s, previously achievable only in self-assembled dots. The properties of the NFDE quantum dots revealed in this study make them a favorable system for electrical spin qubit manipulation with a potential for minimized decoherence effects from the nuclear spin bath.

II. SAMPLES AND TECHNIQUES

The nanohole-filled droplet epitaxial quantum dot sample is grown via solid molecular beam epitaxy. The GaAs buffer growth is followed by deposition of 11 monolayers of Ga at $520\,^\circ$C forming Ga droplets. The droplet is then annealed under As flux resulting in crystallization and eventual formation of nanoholes due to As dissolution and Ga diffusion. The edges of the nanohole typically exhibit moundlike structures along $[\bar{1}10]$ (see AFM images in Fig. 1 in Ref. [22]). The holes are then filled by depositing 7 nm of $Al_{0.44}Ga_{0.56}As$ forming the bottom barrier. This is followed by deposition of 3.5 nm of GaAs resulting in formation of QDs. The dots are then capped by a $112-$nm $Al_{0.33}Ga_{0.67}As$ top barrier and 20-nm GaAs layer. Further details about the growth process can be found in Ref. [22].

Single dot photoluminescence (PL) spectroscopy is performed with a confocal setup which collects low-temperature ($T \approx 4.2$ K) PL from a ~1 μm spot. Magnetic fields up to 10 T along the sample growth axis (Faraday geometry) are employed in this study. The polarization degree of the nuclear spins is probed by measuring hyperfine (Overhauser) shifts in the Zeeman splitting of the quantum dot PL. Nuclear spin polarization and NMR spectroscopy studies are performed using the methods described in Ref. [27].

A typical wide range PL spectrum of the studied structure under nonresonant excitation ($E_{laser} = 1.96$ eV) is shown in Fig. 1(a) at $B_z = 6$ T. Apart from quantum well (QW) emission at $E \approx 1.67$ eV, two spectral distributions of QD emission are observed: one at $E \approx 1.58$ eV (which we denote as type A dots) and one at $E \approx 1.63$ eV (denoted as type B dots). Distinct PL energies are not the only difference: as we demonstrate in this work, type A and B dots have profoundly different carrier g factors and strain profiles, suggesting that the two types of dots have markedly different origin. The most likely origin of the quantum dots (based on the findings discussed below) is demonstrated in Fig. 1(b), where a schematic cross-section structure of the QD sample (based on previous AFM studies [22]) is shown. We attribute QDs type A emitting at $E \approx 1.58$ eV to carrier recombination inside inverted pyramids formed by in-filling with GaAs of the *in situ* etched nanoholes in AlGaAs. The dots of type B are attributed to the localized states formed at the edges of the nanoholes. Such dots have shallower potential and give rise to emission at higher energy $E \approx 1.63$ eV. The corresponding energy band diagram of both type A and B dots is shown schematically in Fig. 1(c).

Typically, we observe emission from 5–10 dots within the excitation spot of ~1 μm^2. While such density is too high to isolate reliably individual dots, it is low enough to observe and interpret fine structures and Zeeman splittings of the emission lines.

All error estimates quoted in the paper are 95% confidence intervals.

III. EXPERIMENTAL RESULTS

In this section, we examine in turn various aspects of the spin properties of NFDE quantum dots.

A. Magnetic properties of single charges: Close-to-zero electron *g* factors

Emission from a neutral QD is a result of recombination of an electron with spin up ↑ (or spin down ↓) and a hole with spin up ⇑ (or spin down ⇓) along Oz growth axis (parallel to magnetic field B_z). An electron-hole pair can form either a "bright" exciton $|\Uparrow \downarrow\rangle$ ($|\Downarrow \uparrow\rangle$) with spin projection $+1$ (-1) or optically forbidden "dark" exciton [28] $|\Uparrow \uparrow\rangle$ ($|\Downarrow \downarrow\rangle$) with spin projection $+2$ (-2). In QDs with nonideal symmetry, the exchange interaction mixes the bright and dark states [28] and hence the dark states gain small oscillator strength and can be observed in QD PL at low excitation powers [28–30].

Figure 2(a) presents a series of PL spectra of QD B1 measured at low excitation power and different B_z. The emission of both dark excitons can be observed at finite B_z: the emission lines are marked with ◇ for $|\Uparrow \uparrow\rangle$ and ▽ for $|\Downarrow \downarrow\rangle$ exciton. A fingerprint feature of a "dark" exciton is its enhanced emission when it anticrosses with a bright state [28]. This is observed in Fig. 2(a) for the $|\Uparrow \uparrow\rangle$ exciton: at $B_z = 3$ T, it has enhanced emission in σ^- polarization due to the mixing
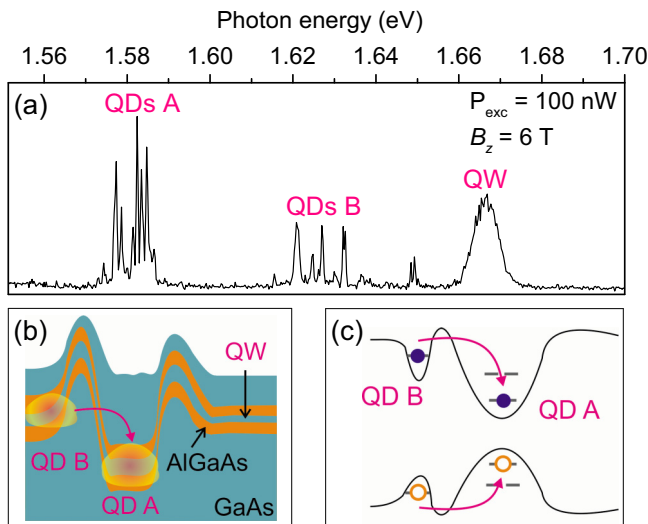

FIG. 1. Nanohole in-filled droplet epitaxial quantum dots. (a) Low-temperature photoluminescence spectrum showing emission from two types of quantum dot (A and B) and a quantum well (QW) measured under nonresonant excitation ($E_{laser}=1.96$ eV) at $B_z= 6$ T. (b) Schematic diagram showing the structure of *in situ* nanohole in-filled droplet epitaxial QDs. The deposited GaAs causes formation of a dot inside the nanohole (QD type A). Additional dots (type B) can be formed at the edge of the nanohole. Quantum well (QW) is formed outside the nanoholes. (c) Schematic band structure of nanohole in-filled dots of type A and B. Arrows depict a possible charge tunneling from dot B to dot A.
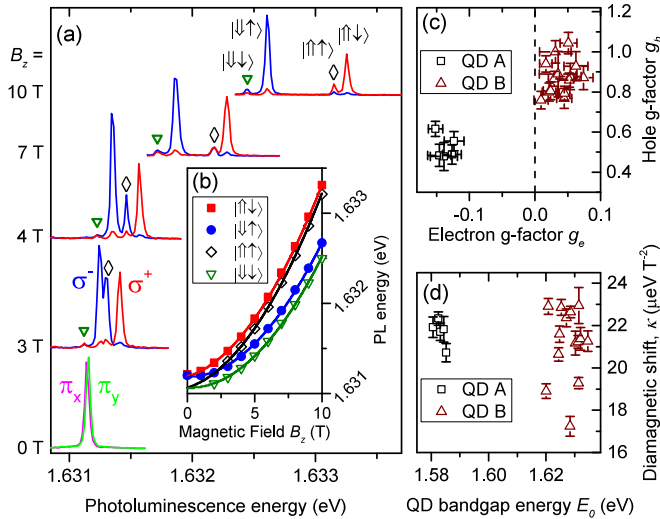
FIG. 2. Magnetophotoluminescence spectroscopy of NFDE quantum dots. (a) Magnetic field B_z dependence of PL emission from bright and dark excitons in a quantum dot B1 under σ^+ low-power ($P_{\text{exc}} = 200$ nW) excitation. Red (blue) lines correspond to spectra recorded in σ^+ (σ^-) polarized detection, while green and magenta correspond to spectra recorded in linear polarizations (π_x, π_y) at $B_z = 0$. The diamonds ($\diamond$) and triangles ($\triangledown$) indicate the weak peaks corresponding to $|\Uparrow\uparrow\rangle$ and $|\Downarrow\downarrow\rangle$ dark excitons, respectively. The two intense peaks correspond to $|\Uparrow\downarrow\rangle$ and $|\Downarrow\uparrow\rangle$ bright excitons. (b) PL energies of dark (open symbols) and bright (full symbols) exciton peaks from (a). The solid lines show fit to the data yielding the electron (hole) g factor $g_e = 0.05$ ($g_h = 0.86$) and diamagnetic shift $\kappa = 21.2$ μeV T^{-2}. (c) Hole g factors (g_h) versus electron g factors (g_e) measured for several QDs type A (squares) and QDs B (triangles) from the same sample. (d) Diamagnetic shifts κ versus QD band-gap energies E_0 for the same dots as in (c). All error bars are 95% confidence intervals.

with $|\Downarrow\uparrow\rangle$, while at $B_z = 10$ T the enhanced emission in σ^+ polarization is caused by mixing with $|\Uparrow\downarrow\rangle$ bright exciton.

The PL peak energies extracted from the data in Fig. 2(a) are shown in Fig. 2(b) by the symbols. The fitting is shown by solid lines. From the fit we find the electron and hole Landé g factors along the Oz axis g_e and g_h and the diamagnetic shift coefficient κ (see Appendix A for details of fitting). We have performed magneto-PL measurements for a set of different individual dots of both types A and B from the same sample. The extracted electron and hole g factors are plotted in Fig. 2(c) together with diamagnetic shifts shown in Fig. 2(d). Surprisingly, for QDs B, g_e have close-to-zero values with an average of $g_e \approx +0.05$, an order of magnitude smaller than for GaAs/AlGaAs QDs formed by natural fluctuation of the quantum well width [29,31]. QDs of type A also have small (and negative) g factors $g_e \approx -0.1$. The values of the diamagnetic shift κ are 17–24 μeV T^{-2} for both type A and B dots, which is larger than in natural GaAs/AlGaAs QDs (10 μeV T^{-2}, Ref. [29]) and DE-grown GaAs/AlGaAs QDs obtained by crystallization of Ga droplets (4–8 μeV T^{-2}, Ref. [20]). We attribute the large diamagnetic shifts of the studied NFDE QDs to their larger lateral dimensions [32]: a typical nanohole size is $\sim$65 nm (Ref. [22]) compared to droplet size $\sim$40 nm in DE-grown dots [33].

Large lateral sizes of the wave functions in the NFDE dots imply that "quenching" of the orbital angular momentum (characteristic for small dots) is negligible [34], and the results of extensive studies on g factors in GaAs/AlGaAs quantum wells [35–40] are directly applicable to NFDE dots. Indeed, we find that the small negative (positive) g_e values observed for QDs type A (B) emitting at $E \approx 1.58$ eV ($E \approx 1.63$ eV) are in good agreement with the "universal" dependence of g_e on quantum well ground-state energy [40]: in particular, there is a close match between $g_e \approx 0$ in dots type B and $g_{e,\parallel} \approx 0$ observed in quantum wells with similar band-gap energy of $E \approx 1.62$ eV. It is thus evident that NFDE dots offer strong 3D carrier confinement with lifetime-limited optical transition linewidths [26] while exhibiting carrier magnetic properties typical for quantum wells, where the g factor of the electron is approximately an average of the g factors in the dot and in the barrier materials weighted by the envelope wave-function density [34,35,37]. (The magnitude of the electron wave-function penetration into the barriers is further discussed in Appendix D.)

Based on our observation of very small $g_e \sim 0.05$ we expect that nanohole etching and subsequent in-filling processes can be optimized to obtain QDs of either type A or type B with average $g_e \approx 0$ (by tuning the ground-state energy similar to quantum wells). The electron g factor g_e in a QD can be tuned via electric field [41]. Therefore, adding electrodes to NFDE QD structures with $g_e \approx 0$ would in principle allow coherent rotation with access to an arbitrary part of the electron spin Bloch sphere by switching the value of the electric field [16,42]. The advantage of this approach over optical manipulation is that a large number of QD spin qubits can be controlled independently by multiple electrodes on the same semiconductor chip. This would allow for scalability, the key requirement on the way for practical implementation of quantum information processing devices.

B. Optical dynamic nuclear polarization (DNP)

Since in III-V semiconductors the electron spin is coupled to the nuclear spin environment via the hyperfine interaction, it is important to understand the properties of the nuclear spin bath and establish techniques for its manipulation. In order to monitor the polarization of the QD nuclei, we measure the splitting $\Delta E_{|\Uparrow\downarrow\rangle,|\Downarrow\uparrow\rangle}$ between the Zeeman components $|\Uparrow\downarrow\rangle$ and $|\Downarrow\uparrow\rangle$ of the bright exciton (we neglect the contribution of the hole hyperfine interaction which is small [43]). The Overhauser shift E_{OHS} is the deviation of $\Delta E_{|\Uparrow\downarrow\rangle,|\Downarrow\uparrow\rangle}$ from its value at fully depolarized nuclei and is a measure of the nuclear spin polarization. The maximum possible Overhauser shift in GaAs with natural 60.1%/39.9% abundance of ^{69}Ga/^{71}Ga is $E_{\text{OHS}}^{\max} = I(A^{(^{75}\text{As})} + 0.601 A^{(^{69}\text{Ga})} + 0.399 A^{(^{71}\text{Ga})}) \approx 127$ μeV, where $A^{(^{75}\text{As})} \approx 43$ μeV, $A^{(^{69}\text{Ga})} \approx 37$ μeV, and $A^{(^{71}\text{Ga})} \approx 48$ μeV are the hyperfine constants [44] of the corresponding isotopes with nuclear spin $I = \frac{3}{2}$. We also define nuclear spin polarization degree $-1 < \sigma_N < 1$ as $\sigma_N = E_{\text{OHS}}/E_{\text{OHS}}^{\max}$. As nuclear spin polarization might be nonuniform within the dot volume, such definition of σ_N gives an average weighted by the electron envelope wave-function density.

We start by investigating the dynamic nuclear polarization (DNP) under optical pumping, in particular, the dependence on
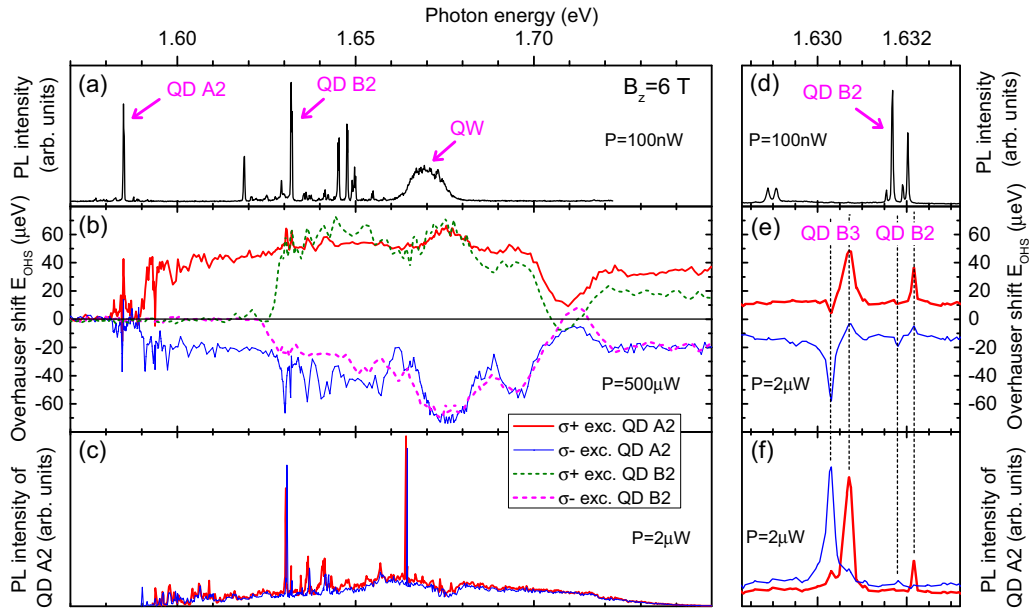
FIG. 3. Polarization-dependent PL, PLE, and DNP spectroscopy on NFDE QDs at $B_z = 6$ T. (a)–(c) Wide range spectra. (a) PL spectrum showing QW, QD A2, and QD B2 emission under nonresonant excitation ($E_{laser} = 1.96$ eV). (b) Overhauser shift measured on dots A2 (blue line for σ^- and red line for σ^+ excitation) and B2 (magenta line for σ^- and green line for σ^+ excitation) as a function of the laser excitation energy E_{laser}. (c) PL emission intensity of QD A2 (red for σ^+ and blue for σ^- excitation) as a function of E_{laser}. (d)–(f) High-resolution spectra. (d) PL spectrum of QD B2. (e) Low-power DNP measured on QD A2 as E_{laser} is scanned close to QD B2 resonance. (f) Zoomed-in view of (c).

the energy of the laser excitation E_{laser}. Figure 3(a) shows the PL spectrum of QD A2 used in these experiments; the emission from type B dots is also observed. A photoluminescence excitation (PLE) spectrum is presented in Fig. 3(c): in this measurement PL was detected from QD A2 and excited at variable E_{laser} with both circular polarizations at low optical power of 2 μW. The PLE data reveal sharp peaks for E_{laser} up to ~1.61 eV, which is ~25 meV above the QD A2 ground-state energy of ~1.585 eV; we ascribe these peaks to the excited states of the QD A2. For E_{laser} above ~1.61 eV, the PLE trace has a broad background. We attribute this to the large lateral size of the type A quantum dots resulting in high spectral density of the excited states merging into a continuum. However, in addition to this broad background there is a set of sharp PLE peaks observed at E_{laser} above 1.63 eV. These have energies close to the energies of the PL peaks of the type B quantum dots, revealing an efficient mechanism for injecting electron-hole pairs into A dots via the excitation of the B dots, as shown schematically in Fig. 1(c).

In addition to PLE spectroscopy, we have measured the nuclear polarization E_{OHS} as a function of E_{laser}. The red (blue) line in Fig. 3(b) shows E_{OHS} induced in QD A2 under σ^+ (σ^-) polarized high-power ($P = 500\,\mu$W) optical excitation. (The measurement was performed with pump-probe techniques described in Appendix C.) The results allow at least three mechanisms of DNP to be identified:

(i) It can be seen that the highest efficiency DNP with $|E_{OHS}| \geqslant 70\,\mu$eV is achieved for $E_{laser} \sim 1.675$ eV corresponding to the QW states: This is similar to DNP via QW states in fluctuation GaAs QDs [10,29,45] and DNP via the wetting layer states in self-assembled dots [11,29].

(ii) A series of sharp peaks between $E_{laser} = 1.585$–1.60 eV is observed correlated with the PLE peaks in Fig. 3(c).

These correspond to DNP via resonant optical excitation either of the QD A2 ground state or excited states (e.g., p shell). Such a mechanism is also well known from the studies on self-assembled quantum dots [46,47]. Similar to the case of PLE, the nonzero background E_{OHS} at $E_{laser} > 1.60$ eV is ascribed to nearly continuum spectrum of the excited states of the NFDE QDs with large lateral dimensions.

(iii) Finally, a set of sharp peaks is observed in Fig. 3(b) at $E_{laser} = 1.63$–1.66 eV. These peaks are strongly correlated to both PLE and PL peaks of the type B QDs, suggesting that DNP in one dot (of type A) can be produced by optical excitation of another dot (of type B). Such a mechanism has not been reported previously and is unique to the NFDE QDs.

In order to understand the mechanism (iii) of the interdot DNP, we perform high-resolution spectroscopy, as shown in Figs. 3(d)–3(f) where we focus on the range of energies around the QD B2 ground excitonic state. Vertical dashed lines show that with high accuracy there is a direct correspondence between the peaks in PLE [Fig. 3(f)] and DNP [Fig. 3(e)] spectra, confirming that the DNP in QD A2 is a result of the resonant optical electron-hole injection into the dot A2. One doublet of the circularly polarized PLE and DNP peaks at 1.632 eV can be attributed to the Zeeman doublet of the QD B2 observed in PL [Fig. 3(d)], albeit there is a small mismatch in energy [48]. This allows the mechanism of the interdot DNP to be explained: Under resonant optical excitation an exciton is generated in QD B2. The exciton can then tunnel into QD A2 and recombine [resulting in a PLE peak in Fig. 3(f)]. With a finite probability, the exciton electron can exchange its spin with a nucleus either during exciton tunneling into QD A2 or during recombination in QD A2 [resulting in a DNP peak in Fig. 3(e)]. At the same time, the much stronger PLE and DNP doublets at 1.630 eV have no PL lines from type B QD related

to them. This however, can be understood if we assume that such a QD (that we denote as B3) exists but has much larger tunneling rate compared to QD B2. Thus, the excitons from QD B3 tunnel into QD A2 before they can recombine, and as a result the PL from QD B3 is suppressed while PL and DNP in QD A2 are enhanced.

We have also measured the DNP in QD B2 as a function of E_{laser}, as shown in Fig. 3(b) by the dashed lines. Importantly, there is no DNP in QD B2 when exciting QD A2: we thus conclude that the nuclear spin diffusion between the dots is negligible and the interdot DNP in QD A2 under resonant optical excitation of QD B2 is indeed due to mechanism (iii), the tunneling of the excitons.

Upon examining several QDs from the same sample, we found that the results presented in Fig. 3 are well reproduced in other dots. The DNP in dots of type A induced via resonant pumping [mechanism (ii)] is found to be as large as $|E_{OHS}| \approx 50\ \mu eV$. The DNP induced via optical pumping into the QW [mechanism (i)] or via tunneling from type B dots [mechanism (iii)] is even larger $|E_{OHS}| \approx 85\ \mu eV$, corresponding to polarization degrees of $\sigma_N \approx 67\%$. However, the DNP via interdot tunneling may have an advantage since it allows for a selective control of the nuclear polarization in individual dots, while nonresonant excitation of the QW polarizes nuclei in all dots within the laser spot [1,29]. The DNP was found to be the most efficient at high magnetic fields ($B_z \sim 6$–10 T), however, significant nuclear polarization could be induced at B_z as small as 0.5 T (see additional results on B_z dependence in Appendix B).

Finally, we note that the three DNP mechanisms (i)–(iii) identified here provide classification in terms of distinct optical absorption paths that lead to the buildup of nuclear spin polarization. By contrast, establishing the exact microscopic DNP mechanisms is a much more difficult task. The key factor governing DNP processes is that electron (or exciton) Zeeman energy is always much larger than the nuclear Zeeman energy (even for very small electron g factors observed here in NFDE dots), so that DNP via direct electron-nuclear spin flip-flop is very inefficient. Efficient DNP mechanisms are usually associated with second-order processes, where the mismatch in electron and nuclear Zeeman energies is compensated by some reservoir such as photons, phonons, or tunneling coupling to electron Fermi sea. In special cases, individual microscopic DNP mechanisms can be identified (e.g., hyperfine-assisted resonant absorption by forbidden optical transitions in positively charged dots [49] or hyperfine-assisted recombination of nonresonantly excited dark states in neutral dots [50]), while in other cases two or more competing mechanisms play a significant role (e.g., Overhauser and reverse-Overhauser mechanisms under resonant optical pumping of negatively charged dots [47]). The exact microscopic processes responsible for each of the three optical DNP mechanisms (i)–(iii) observed here in NFDE dots are yet to be identified and require further work.

C. Nuclear magnetic resonance spectroscopy: Probing quantum dot internal structure

The ability to induce large DNP allows us to perform QD nuclear magnetic resonance (NMR) spectroscopy [27,51,52]
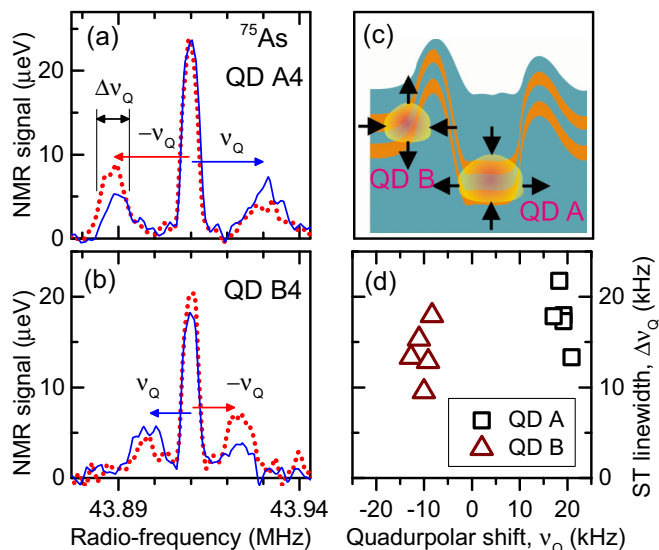

FIG. 4. Nuclear magnetic resonance (NMR) spectroscopy. (a), (b) Inverse NMR spectra of ^{75}As nuclei measured on QD A4 (a) and QD B4 (b) under σ^+ (red dotted lines) and σ^- (blue solid lines) optical nuclear spin pumping. The satellite transitions (STs) are separated from the central transition (CT, observed at $\nu \approx 43.91$ MHz) by the strain-induced quadrupolar shift $\pm\nu_Q$. The central transition width is resolution limited (6 kHz) while the ST widths are $\Delta\nu_Q$. (c) Schematic showing the strain profile in dots A and B with black arrows indicating the strain directions for both dots as deduced from the NMR spectra in (a) and (b). (d) Quadrupolar shifts ν_Q and ST widths at half maximum $\Delta\nu_Q$ measured for several QDs type A (squares) and B (triangles).

(using "inverse" NMR techniques [27]) in order to investigate the QD structural properties. Figures 4(a) and 4(b) show NMR spectra of the ^{75}As spin $I = \frac{3}{2}$ isotope for QDs A4 and B4, respectively. In addition to ^{75}As, we have successfully observed NMR signals of ^{69}Ga and ^{71}Ga (not shown), while no signal from ^{27}Al could be detected (see further discussion in Appendix D). The ^{75}As spectra shown in Figs. 4(a) and 4(b) are dominated by narrow (resolution-limited) central peaks corresponding to the nuclear spin $-1/2 \leftrightarrow +1/2$ central transitions (CTs). Two satellite transitions (STs) $+1/2 \leftrightarrow +3/2$ and $-3/2 \leftrightarrow -1/2$ are shifted from the CT by $+\nu_Q$ and $-\nu_Q$, respectively (this definition sets our convention for the sign of the nuclear quadrupolar frequency ν_Q). The nonzero ν_Q reveals the presence of a shear (nonhydrostatic) elastic strain, even though the GaAs/AlGaAs structures are expected to be nearly lattice matched [19].

In order to quantify the strain in QDs, we first note an asymmetry observed in the NMR spectra of Figs. 4(a) and 4(b): under σ^+ optical pumping the low-frequency (high-frequency) ST of QD A4 (QD B4) has increased amplitude. As σ^+ light enhances the NMR signal of the $-3/2 \leftrightarrow -1/2$ ST [27], we conclude that QD A4 and QD B4 have opposite signs of the quadrupolar shifts: $\nu_Q > 0$ for QD A4 and $\nu_Q < 0$ for QD B4. NMR measurements on several individual dots shown in Fig. 4(d) reveal systematic positive values $\nu_Q \approx +20$ kHz for type A dots (squares) and negative values $\nu_Q \approx -10$ kHz for type B dots (triangles). The ST half-widths $\Delta\nu_Q$, reflecting the inhomogeneous distribution of ν_Q within the dot, are found to

vary in the range $\Delta\nu_Q \sim 10$–20 kHz. The quadrupolar effects in the NFDE dots are nearly three orders of magnitude smaller than in self-assembled dots (tens of kHz compared to several MHz for ^{75}As nuclei [27]).

Pure hydrostatic strain does not cause nuclear quadrupolar shifts, while shear strain induces quadrupolar shifts dependent on the orientations of the strain tensor axes with respect to magnetic field. In planar QD structures studied here in Faraday geometry the major contribution arises from the uniaxial strain with major axis parallel to magnetic field (along Oz). The magnitude of the strain can be characterized with $\epsilon_b = \epsilon_{zz} - (\epsilon_{xx} + \epsilon_{yy})/2$, so that $\epsilon_b > 0$ describes a tensile strain along Oz ($\epsilon_{zz} > 0$) with corresponding compressive deformation perpendicular to Oz ($\epsilon_{xx} < 0, \epsilon_{yy} < 0$). The quadrupolar shift corresponding to such ϵ_b is

$$\nu_Q = \frac{3eQS_{11}\epsilon_b}{2hI(2I-1)}, \tag{1}$$

where Q is the nuclear quadrupolar moment ($\approx 0.31 \times 10^{-28}$ m^2 for ^{75}As), $|S_{11}| \approx 3.9 \times 10^{22}$ V m^{-2} is the gradient elastic tensor for ^{75}As in bulk GaAs (the sign of S_{11} is undefined) [53], e is electron charge, and h is the Planck's constant. Thus, the average NMR frequency shift ν_Q provides a direct measure of the average strain, while the ST linewidth $\Delta\nu_Q$ gives a measure of the strain distribution within the quantum dot.

In order to derive structural information from the NMR spectra, we make a comparison with previous studies on self-assembled dots. In disk-shaped (large lateral and small vertical dimensions) self-assembled InGaAs/GaAs quantum dots ϵ_b is positive (tensile strain along the Oz axis) [54]. In such dots, negative ν_Q was found for ^{75}As nuclei, implying $S_{11} < 0$ for the sign convention on ν_Q adopted in this work [27]. For GaAs/AlGaAs NFDE QDs type A we find positive ν_Q, and hence ϵ_b derived from Eq. (1) is negative (compressive along Oz): $\epsilon_b = -0.014\%$. This, however, is expected for disk-shaped dots since the GaAs lattice constant is smaller than that of AlGaAs (as opposed to InGaAs/GaAs pair). By contrast, for type B QDs we find anomalous positive $\epsilon_b = 0.007\%$ (tensile strain along Oz). In order to verify further the relation between the signs of ν_Q and ϵ_b, we have conducted additional NMR measurements in a sample that was stressed compressively along the [110] direction, which increases ϵ_b: As expected ν_Q was reduced, observed as sign reversal of ν_Q in dots type A, and increased $|\nu_Q|$ in dots type B.

Most importantly, in each dot we observe either distinctly positive ϵ_b (QDs type B) or distinctly negative ϵ_b (QDs type A). This allows us to conclude that the overlap between the excitonic wave functions in type A and B dots is small, as large overlap would have resulted in a gradual transition between tensile and compressive strains leading to large inhomogeneous broadening $\Delta\nu_Q$ of the NMR spectra (as observed in self-assembled dots [27]). We argue that distinctly different characteristic NMR spectra are a sign of the different origin and structure of dots type A and B.

We provide the following most likely explanation that consistently accounts for the NMR data. We assume the structure of the dots is as shown in Fig. 1(b) and in Fig. 4(c): while type A QDs are formed by in-filling of the nanohole, the "mounds" formed at the rim of the nanohole (and previously

observed in AFM [22]) create additional sites with a 3D confinement resulting in formation of type B QDs. The tensile strain along Oz observed in type B QDs can then be explained by the effect of the "sloped" AlGaAs barriers exerting pressure on the GaAs layer and resulting in its compressive in-plane deformation as shown by the arrows in Fig. 4(c). By contrast, the topology of type A QDs in the nanohole is closer to that of a quantum well, so that both AlGaAs barriers act to stretch the GaAs layer in the horizontal plane resulting in compressive strain along Oz ($\epsilon_b < 0$). However, estimating the strain in an ideal GaAs/Al$_{0.4}$Ga$_{0.6}$As quantum well [using Eq. (3a) of Ref. [55]] at low temperature we find a negative ϵ_b with much bigger absolute value $\epsilon_b \approx -0.1\%$. This suggests that in both QDs A and B there is a significant degree of additional in-plane compression resulting most likely from the concave shapes of the dots. This additional in-plane compression is sufficiently large to overcome the intrinsic stretching (arising from the lattice mismatch of GaAs and AlGaAs) and give rise to $\epsilon_b > 0$ in dots type B, while in dots type A it leads to negative ϵ_b but of much smaller magnitude compared to quantum wells.

The dot morphology shown in Fig. 4(c) is a most likely explanation since it agrees well with PL, PLE, DNP, and NMR spectroscopy results reported here, as well as with earlier AFM studies. While the dot density of the structure studied in detail in this work does not allow reliable isolation of individual dots, our preliminary studies on a similar structure with very low nanohole density have shown that emission of dots type B is observed only together with emission from a dot of type A. This further strengthens our interpretation of the quantum dot morphology in nanohole-filled structures.

Finally, we note that the small values of ϵ_b derived from the NMR spectra confirm that the nearly zero g factors of the NFDE dots are not related to strain effects, especially since the impact of strain on the electron g factors is known to be small even in structures with much larger lattice mismatch [39].

D. Long nuclear spin relaxation times

Stability of the nuclear spin bath polarization is crucial for achieving long carrier spin coherence times in quantum dots. The lifetime of the quantum dot nuclear spin state is ultimately limited by its relaxation time in the dark $T_{1,N}$, which is controlled by nuclear spin diffusion, and charge fluctuations in the dot or in nearby dots and charge traps. In order to investigate $T_{1,N}$ in NFDE dots, we perform measurements using *pump-wait-probe* protocol, where the dark waiting time Δt is systematically changed, keeping all the other parameters fixed (the timing diagram is shown in the inset of Fig. 5). The dependence of the Overhauser shift on Δt is shown in Fig. 5 for two quantum dots: QD A6 (open circles, measured with σ^+ pump) and QD B6 (full circles, measured with σ^- pump).

The solid lines show the exponential fits to the data revealing very long $T_{1,N} = 7800$ s for QD A6 and $T_{1,N} = 4900$ s for QD B6. At the same time, it can be seen that some of the experimental points (marked with dotted circles) deviate significantly from the exponential decay. Unlike other points, these were measured *after* measuring the points with very long $\Delta t > 1000$ s; such deviation is a result of nuclear
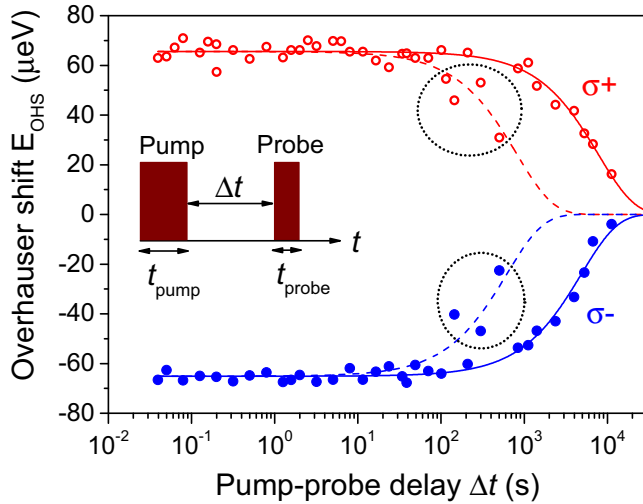
FIG. 5. Decay dynamics of the nuclear spin polarization in the dark measured using *pump-wait-probe* protocol (with timing diagram shown in the inset). Overhauser shift is probed at varying delay Δt between pump ($t_{pump} = 6.5$ s) and probe ($t_{probe} = 0.25$ s) for two different quantum dots. The data measured with σ^+ pump (red open circles) are for QD A6 while the data with σ^- pump (blue full circles) are for QD B6. The solid lines are exponential fits to the data revealing $T_{1,N} = 7800$ s for QD A6 and $T_{1,N} = 4900$ s for QD B6. The dashed lines are the fits to the data points which were recorded after keeping the QD in the dark for durations longer than 1000 s (highlighted with circles), which reduces the effect of nuclear spin diffusion on the subsequent pump-probe cycle resulting in shorter decay times $T_{1,N} \approx 860$ s for QD A6 and $T_{1,N} \approx 640$ s for QD B6.

spin diffusion. Indeed, when QD is repeatedly excited by the circularly polarized light of the same helicity, the nuclei in the surrounding of the dot become polarized, suppressing the spin diffusion [56] and resulting in extended $T_{1,N}$. Although systematic study of the nuclear spin diffusion is beyond the scope of this work, an estimate of the nuclear spin decay time excluding the effect of polarized nuclear spin surrounding can be obtained by fitting the data points marked with the dashed circles and excluding other points measured at longer Δt. This way, we find $T_{1,N} \approx 860$ s for QD A6 (dashed red line) and $T_{1,N} \approx 640$ s for QD B6 (dashed blue line). Even though these decay times exclude the effect of the dot environment polarized via spin diffusion, they are still significantly longer than $T_{1,N} \sim 40$ s reported for monolayer fluctuation GaAs/AlGaAs QDs [45]: the stability of the nuclear spin bath in NFDE dots is close to that of self-assembled InGaAs/GaAs and InP/GaInP QDs [30,56–58].

The stability of the nuclear spin polarization in the NFDE QDs can be explained from the NMR spectra shown in Figs. 4(a) and 4(b). In contrast to the natural fluctuation GaAs/AlGaAs QDs [45,59], the satellite transitions (STs) of the NMR spectra are clearly spectrally separated from the central transition (CT) in NFDE QDs. Such separation implies that the spin exchange between the neighboring nuclei is strongly inhibited. For example, in the natural GaAs/AlGaAs QDs, where all the nuclear spin transitions are degenerate, a nuclear spin in a $I_z = +\frac{3}{2}$ state can flip into the $I_z = +\frac{1}{2}$ and transfer the excess polarization to the adjacent spin which will

flip from $I_z = -\frac{1}{2}$ to $I_z = +\frac{1}{2}$ state. By contrast, in the NFDE QDs such process would be suppressed due to the energy mismatch of the $-1/2 \leftrightarrow +1/2$ (CT) and $+1/2 \leftrightarrow +3/2$ (ST) transitions. The reduced spin exchange rate in the NFDE QDs slows down the propagation of nuclear spin polarization into the AlGaAs barrier, thus increasing the lifetime of the nuclear spin magnetization inside the QD.

We thus demonstrate that NFDE dots offer excellent stability of the nuclear spin bath, crucial for achieving long electron and hole spin coherence but found previously only in highly strained self-assembled dots [30,56–58].

IV. DISCUSSION AND CONCLUSIONS

In conclusion, we have explored electron and nuclear spin properties of *in situ* nanohole-filled droplet epitaxial (NFDE) quantum dots and identified several unique properties of such dots:

(i) Investigations into the Landé g factors have demonstrated a quantum dot system with electron g factor g_e approaching zero, which agrees well with previous observations on GaAs/AlGaAs quantum wells with similar ground-state energies. Thus, we demonstrate a system that possesses all the advantages of quantum dots (strong 3D confinement, lifetime limited optical transition linewidths) while offering a simple way to control electron g factor by changing the GaAs layer thickness (well established for quantum wells [35–37]). The close-to-zero g_e values offer a potential route to all-electrical spin control, making NFDE dots a promising platform for scalable quantum information circuits.

(ii) The nuclear spin bath can be controlled optically with average polarization degrees as large as 65% achieved reliably.

(iii) NMR spectroscopy reveals small elastic strain which nevertheless has a major impact on the nuclear spin system of NFDE dots resulting in very long nuclear spin lifetimes comparable to those observed previously only in self-assembled InP [30] and InGaAs [56] QDs. Furthermore, we note that most recently it has been shown that nuclear quadrupolar effects are a major source of decoherence of the electron spin in self-assembled quantum dots [14,15], in particular at low magnetic fields where nuclear quadrupolar effects dominate over the Zeeman effect. Thus, NFDE quantum dots could be an excellent alternative to self-assembled InGaAs dots since quadrupolar induced decoherence of the electron spin would be eliminated, while the very stable nuclear spin bath characteristic of self-assembled structures is maintained.

(iv) Using NMR spectroscopy, two types of quantum dots are shown to have opposite signs of strain (tensile or compressive along the growth axis). We propose an explanation based on two distinct processes leading to dot formation: in-filling of the nanoholes and formation of GaAs dots at the edges of the nanoholes.

APPENDIX A: SINGLE CARRIER *g*-FACTOR MEASUREMENTS: DATA ANALYSIS PROCEDURE

The B_z-dependent peak energies of bright (E_b) and dark excitons (E_d) in Fig. 2(b) are fitted using the following equations:

$$E_b = E_0 + [\kappa + \kappa^{(1)}B_z]B_z^2 + \tfrac{1}{2}\delta_0$$
$$\pm \tfrac{1}{2}\sqrt{\delta_b^2 + \mu_B^2[g_h + g_h^{(1)}B_z - g_e]^2 B_z^2},$$

$$E_d = E_0 + [\kappa + \kappa^{(1)}B_z]B_z^2 - \tfrac{1}{2}\delta_0$$
$$\pm \tfrac{1}{2}\mu_B[g_h + g_h^{(1)}B_z + g_e]B_z, \qquad (A1)$$

where μ_B is the Bohr magneton, E_0 is the QD band-gap energy, g_e is the electron *g* factor, δ_0 is the splitting between bright and dark exciton doublets, δ_b is the bright exciton fine-structure splitting, and dark exciton splitting is neglected. Equations (A1) are obtained from the equations of Refs. [28,60] by substituting the constant diamagnetic shift and hole *g* factor with magnetic-field-dependent ones $\kappa + \kappa^{(1)}B_z$ and $g_h + g_h^{(1)}B_z$, respectively.

The importance of using the B_z-dependent corrections to diamagnetic shift and hole *g* factor can be understood by examining the fitting residuals shown in Fig. 6 for the experimental data measured for QD B1 and shown in Fig. 2(b). Symbols in Fig. 6(a) show the residuals of the fitting where B_z-dependent corrections are neglected [by setting $\kappa^{(1)} = 0$, $g_h^{(1)} = 0$ in Eq. (A1)]. There are pronounced systematic errors $\sim \pm 50 \,\mu$eV. By using B_z-dependent diamagnetic shift $\kappa^{(1)}$ as a fitting variable, the systematic errors are reduced to $\sim \pm 20 \,\mu$eV as demonstrated in Fig. 6(b). The remaining systematic errors clearly have opposite signs for the excitons with hole spins ⇑ and ⇓ and can be eliminated using the B_z-dependent hole *g* factor $g_h^{(1)}$ as a fitting parameter as demonstrated in Fig. 6(c). Recent work on shallow InGaAs QDs attributed similar observations of nonlinear Zeeman splitting to the hole *g* factor strongly affected by the heavy-hole–light-hole mixing [61]. In the case of NFDE dots, the nonlinear Zeeman splitting most likely arises from the relatively large lateral dimensions (60–70 nm along [110] and 45 nm along [1̄10], respectively [22]) of these dots favoring heavy-hole–light-hole mixing.

We find the following fitted electron *g*-factor values for QD B1: $g_e \approx 0.054 \pm 0.041$ with $\kappa^{(1)}$ and $g_h^{(1)}$ set to zero, $g_e \approx 0.053 \pm 0.023$ with variable $\kappa^{(1)}$, and $g_e \approx 0.052 \pm 0.009$ with both $\kappa^{(1)}$ and $g_h^{(1)}$ variables. It can be seen that similar g_e values are obtained from the fitting including and neglecting $\kappa^{(1)}$ and $g_h^{(1)}$, however, using B_z-dependent corrections as fitting variables results in more accurate estimates. The other parameters derived from the fit with variable $\kappa^{(1)}$ and $g_h^{(1)}$ are as follows: $E_0 = 1.631\,143 \pm 4 \times 10^{-6}$eV, $\delta_0 = 122 \pm 3\mu$eV, $\kappa = 21.2 \pm 0.3\mu$eV T^{-2}, $\kappa^{(1)} = -0.35 \pm 0.03\mu$eV T^{-3}, $\delta_b = 12.7 \pm 13.2\mu$eV, $g_h = 0.86 \pm 0.04$ and $g_h^{(1)} = 0.031 \pm 0.004$ T^{-1}. The solid lines in Fig. 2(b) show fitting of the data using Eq. (A1) with these
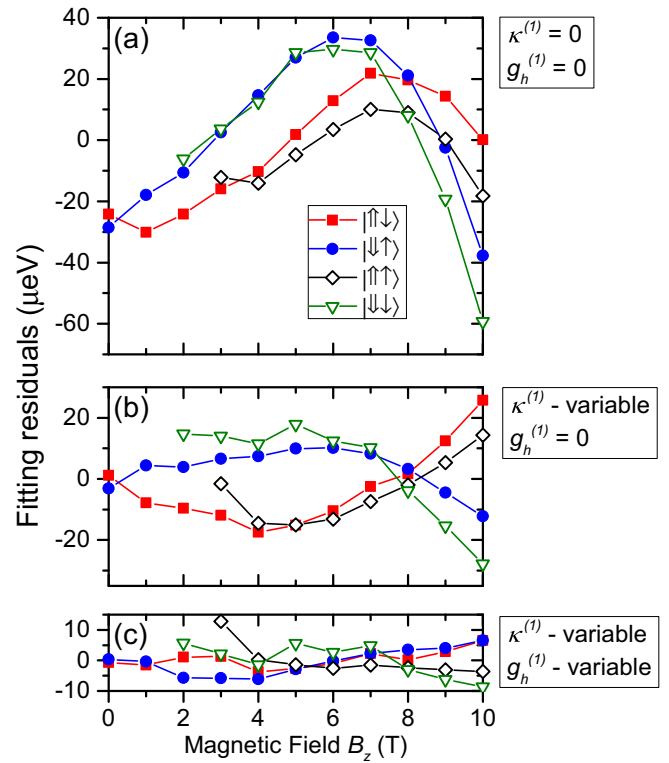

FIG. 6. Symbols show the fitting residuals [the difference between experimental data in Fig. 2(b) and calculations using Eq. (A1)] for all four excitonic states as a function of magnetic field B_z. (a) Fitting without linear corrections [achieved by setting $\kappa^{(1)} = 0$, $g_h^{(1)} = 0$ in Eq. (A1)] results in large systematic errors of $\sim \pm 50 \,\mu$eV. (b) Fitting with variable diamagnetic shift correction $\kappa^{(1)}$ reduces systematic errors down to $\sim \pm 20 \,\mu$eV. (c) Fitting with variable diamagnetic shift $\kappa^{(1)}$ and hole *g*-factor $g_h^{(1)}$ corrections effectively eliminates systematic errors: the resulting residuals $\lesssim \pm 10 \,\mu$eV are within the accuracy with which the energies of the PL peaks in Fig. 2(a) are determined.

parameters. The electron and hole *g* factors g_e and g_h of other dots plotted in Fig. 2(c) are derived using the same fitting procedure with variable $\kappa^{(1)}$ and $g_h^{(1)}$.

APPENDIX B: DEPENDENCE OF DYNAMIC NUCLEAR POLARIZATION (DNP) ON EXTERNAL MAGNETIC FIELD B_z

In order to further investigate the nature of DNP in NFDE QDs, we present a series of excitation power-dependent measurements at varying magnetic fields B_z for QD A7. The DNP is induced by the cw pump laser ($E_{\text{laser}} = 1.642$ eV) tuned in resonance with one of the type B quantum dots. The result is shown for both σ^+ and σ^- excitations as contour plots in Figs. 7(a) and 7(b), respectively. Both plots clearly demonstrate that at high powers ($P_{\text{exc}} \geqslant 10 \,\mu$W) DNP can be induced in a wide range of magnetic fields with maximum magnitudes of $E_{\text{OHS}} = 65 \,\mu$eV ($E_{\text{OHS}} = -55 \,\mu$eV) achieved for this dot at $B_z = 8$–9 T ($B_z = 3$ T) under σ^+ (σ^-) excitation.

At the same time, at high magnetic field ($B_z \approx 9$ T) significant DNP with $|E_{\text{OHS}}|$ as large as 50 μeV is observed
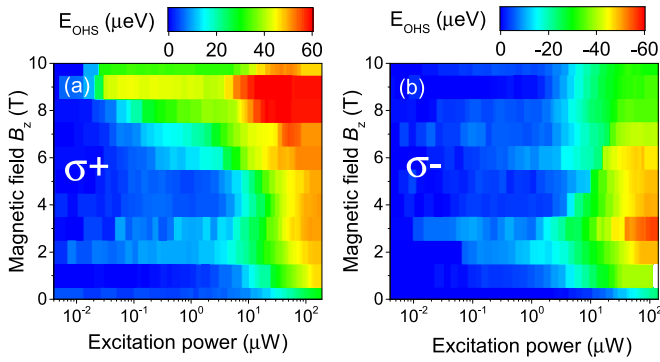
FIG. 7. Magnetic field dependence of the optically induced nuclear spin polarization. Contour plots of the Overhauser shift E_{OHS} in the parameter space of excitation power P_{exc} and magnetic field B_z for σ^+ (a) and σ^- (b) excitation for QD A7. The color scheme on top of each plot depicts the corresponding scale of E_{OHS}.

FIG. 8. Buildup dynamics of the optically induced nuclear spin polarization. The Overhauser shift E_{OHS} is shown as a function of pump pulse duration for σ^+ (red open circles) and σ^- (blue filled circles) pump polarization measured for QD A5 at $B_z = 6$ T. The solid lines show exponential fits to the data with buildup times of $t_{buildup} \approx 790$ ms (590ms) for σ^+ (σ^-) pumping. The inset shows the timing diagram of the *erase-pump-probe* cycle.

under σ^+ excitation at low powers down to $P_{exc} \geqslant 50$ nW. Such low-power DNP has been observed previously in neutral quantum dots in different material systems [29,50], and was shown to be a result of DNP induced by the long-lived dark exciton recombining via second-order process involving a nuclear spin flip.

APPENDIX C: NUCLEAR SPIN PUMP-PROBE SPECTROSCOPY

Dynamical nuclear polarization, nuclear spin decay, and nuclear magnetic resonance measurements presented in the main text are performed using "pump-probe" method [27,43]. Each spectrum is a result of several pump-probe cycles where an optical pump laser pulse induces DNP in the QD, while a probe laser pulse is used to excite and collect PL from the QD and deduce nuclear spin polarization from the Zeeman splitting $\Delta E_{|\Uparrow\downarrow\rangle,|\Downarrow\uparrow\rangle}$. The pump pulse has a high optical power (P_{exc} more than 10 times the saturation power of the QD ground-state emission) and is circularly polarized. The pump pulse duration t_{pump} is sufficiently longer than the nuclear spin buildup time $\tau_{buildup}$ (see discussion following), which ensures a saturated steady-state initial nuclear polarization. For the measurements presented here, the pump duration is 5–7 s, long enough to achieve close to maximum DNP.

The DNP generated during the pump process is probed via a low optical power probe pulse after a time delay Δt. The probe pulse duration t_{probe} is individually selected for each QD such that the nuclear depolarization caused by the probe pulse is less than 3% of the induced DNP. The probe laser is linearly polarized with $E_{laser} = 1.96$ eV and with excitation power 0.2–0.3 of the saturation power of the ground-state QD emission. $t_{probe} = 50$–300 ms are employed in this study. In NMR measurements, a radio-frequency (rf) pulse of duration $t_{rf} = 150$ ms follows the pump and precedes the optical probe [27]. The frequency ν of the rf pulse is changed while the probe spectrum is used to measure E_{OHS}, thus yielding the NMR spectrum $E_{OHS}(\nu)$.

Nuclear spin buildup time $\tau_{buildup}$ depends on the experimental conditions: externally applied B_z, optical excitation 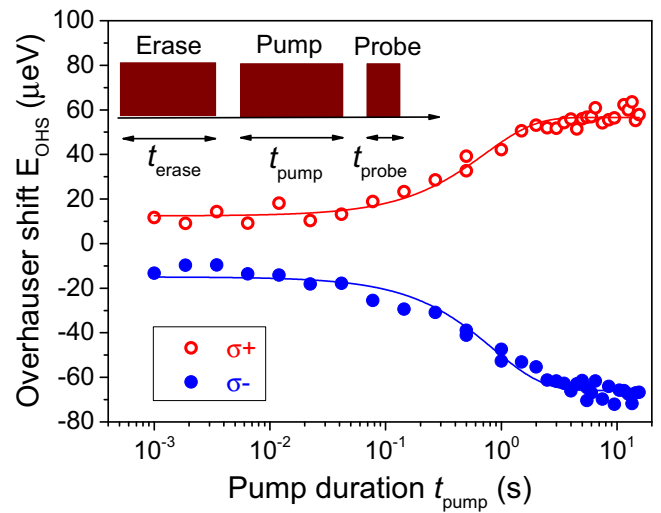power, and the number of nuclei in the dot. We perform pump-probe measurements to determine $\tau_{buildup}$ (see the inset of Fig. 8 for the pump-probe cycle diagram). A linearly polarized erase laser pulse ($t_{erase} = 3.5$ s) is used to depolarize the nuclear spins at the start of each pump-probe cycle. The t_{pump} is varied keeping t_{erase} and t_{probe} constant. The t_{probe} in this measurement is kept at 50 ms, short enough to prevent probe-induced nuclear depolarization. The recorded E_{OHS} as a function of t_{pump} is shown in Fig. 8 at $B_z = 6$ T for two circular polarizations of the pump laser. The exponential fitting reveals $t_{buildup} \approx 700$ ms. In earlier studies, nuclear spin buildup times were found to range from few milliseconds to few seconds in InAs/GaAs self-assembled dots at $B_z = 0 - 1$ T (Refs. [62,63]), few seconds in GaAs/AlGaAs quantum well fluctuation dots at $B_z = 1 - 2$ T (Refs. [45,64]), and few seconds in InP/GaInP at $B_z \geqslant 2$ T (Ref. [30]). Our values of $t_{buildup}$ in NFDE GaAs/AlGaAs QDs are close to the buildup times reported for droplet epitaxial grown GaAs/AlAs QDs formed by Ga droplet crystallization [19] ($\tau_{buildup} = 600$ ms at $B_z = 2.5$ T).

APPENDIX D: PROBING CONTRIBUTIONS OF DIFFERENT ISOTOPES TO THE OVERHAUSER SHIFT

Here, we compare the estimates of the relative concentration of aluminium within the volume of the electron wave function obtained using NMR spectroscopy and the measurements of the electron g factors.

In GaAs/Al$_x$Ga$_{1-x}$As quantum wells, the electron g factor can be accurately approximated as a weighted average of the well material g_e^{GaAs} and the barrier material g_e^{AlGaAs} (Ref. [35]): $g_e = \theta_{AlGaAs}g_e^{AlGaAs} + (1 - \theta_{AlGaAs})g_e^{GaAs}$, where $\theta_{AlGaAs} \in [0,1]$ is the portion of the electron wave-function density within the barriers. The bulk g factors are $g_e^{GaAs} \approx -0.44$ (Refs. [65,66]) and $g_e^{AlGaAs} \approx +0.6$ for GaAs/Al$_x$Ga$_{1-x}$As with $x = 0.4$ (Refs. [66,67]). Due to
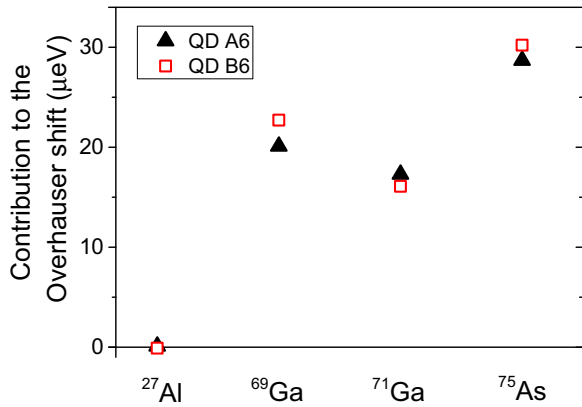
FIG. 9. Contributions to the nuclear spin polarization (total Overhauser shift) of the individual isotopes measured in QD A6 (triangles) and QD B6 (squares). The contributions are obtained by selective depolarization of each isotope after optical DNP induced by a σ^- polarized pump laser.

their large lateral dimensions, we can apply this approach to the NFDE dots. The experimentally observed g factors are $g_e \approx -0.1$ in QDs A and $g_e \approx +0.05$ in QDs type B, as shown in Fig. 2(c). This indicates that the portion of the electron wave function within the barriers is $\theta_{\mathrm{AlGaAs}} \approx 33\%$ ($\theta_{\mathrm{AlGaAs}} \approx 47\%$) in QDs type A (QDs type B). We then calculate the ratio of Al/Ga contained within and weighted by the electron wave function $\rho^{\mathrm{Al}}/\rho^{\mathrm{Ga}} = x \; \theta_{\mathrm{AlGaAs}}/[(1-x)\theta_{\mathrm{AlGaAs}} + (1 - \theta_{\mathrm{AlGaAs}})]$ and find $\rho^{\mathrm{Al}}/\rho^{\mathrm{Ga}} \approx 13\%/87\%$ (19%/81%) in QDs type A (QDs type B).

On the other hand, optically induced Overhauser shift E_{OHS} includes contributions from all the isotopes present within the electron wave function of the QD. In order to separate these contributions, we use resonant rf excitation. We perform measurements at $B_z = 6$ T, where a 5-s long optical pump pulse is followed by a 1.2-s long rf pulse which selectively erases the polarization of a chosen isotope. The rf pulse has a rectangular-shaped spectral band with a 400-kHz width, broad enough to cover the central and both satellite NMR transitions. This ensures that all nuclear spin transitions (corresponding to all I_z) of a selected isotope are excited by the rf field simultaneously resulting in complete depolarization of the chosen isotope. The resulting E_{OHS} is then subtracted from E_{OHS} in a measurement without rf to deduce the magnitude of the optically induced nuclear spin polarization of the selected isotope. We probe depolarization magnitudes of ^{27}Al, ^{69}Ga, ^{71}Ga, and ^{75}As: the results are shown in Fig. 9 with symbols for QD A6 and QD B6. The total Overhauser shift is a sum of all contributions $E_{\mathrm{OHS}}^{\mathrm{total}} = E_{\mathrm{OHS}}^{(^{27}\mathrm{Al})} + E_{\mathrm{OHS}}^{(^{69}\mathrm{Ga})} + E_{\mathrm{OHS}}^{(^{71}\mathrm{Ga})} + E_{\mathrm{OHS}}^{(^{75}\mathrm{As})}$ found to be 66 μeV

(69 μeV) for QD A6 (QD B6). Using the hyperfine constants quoted in Sec. III B we can calculate average polarization degrees for individual isotopes. Averaging over two dots, we find $\sigma_N \approx 64\%$ for ^{69}Ga, $\sigma_N \approx 58\%$ for ^{71}Ga, and somewhat smaller $\sigma_N \approx 46\%$ for ^{75}As.

On the other hand, as it follows from Fig. 9, there is no measurable Overhauser shift contribution from aluminium within the experimental error $E_{\mathrm{OHS}}^{(^{27}\mathrm{Al})} < 2$ μeV. We now use the relative amounts of Al and Ga $\rho^{\mathrm{Al}}/\rho^{\mathrm{Ga}}$ derived above from electron g factors to estimate the expected aluminium Overhauser shift. If we assume that ^{27}Al has the same polarization degree σ_N as ^{69}Ga, $E_{\mathrm{OHS}}^{(^{27}\mathrm{Al})}$ can be estimated by scaling the Overhauser shift $E_{\mathrm{OHS}}^{(^{69}\mathrm{Ga})}$ in the following way: $E_{\mathrm{OHS}}^{(^{27}\mathrm{Al})}/E_{\mathrm{OHS}}^{(^{69}\mathrm{Ga})} = \frac{\rho^{\mathrm{Al}}I^{\mathrm{Al}}A^{(^{27}\mathrm{Al})}}{0.601\rho^{\mathrm{Ga}}I^{\mathrm{Ga}}A^{(^{69}\mathrm{Ga})}}$, where 0.601 is the natural abundance of ^{69}Ga. There is no literature available on ^{27}Al hyperfine constant $A^{(^{27}\mathrm{Al})}$; this, however, can also be estimated by scaling the $A^{(^{69}\mathrm{Ga})}$ constant. For that we take into account that a hyperfine constant is simply a product of the nuclear gyromagnetic ratio, electron Bloch wave-function density at the nucleus, and a set of fundamental constants [44]. As a rough estimate, we assume that the wave-function density at the nucleus is proportional to the atomic weight Z. This way, we finally obtain

$$E_{\mathrm{OHS}}^{(^{27}\mathrm{Al})}/E_{\mathrm{OHS}}^{(^{69}\mathrm{Ga})} = \frac{\rho^{\mathrm{Al}}I^{\mathrm{Al}}\gamma^{(^{27}\mathrm{Al})}Z^{(^{27}\mathrm{Al})}}{0.601\rho^{\mathrm{Ga}}I^{\mathrm{Ga}}A^{(^{69}\mathrm{Ga})}\gamma^{(^{69}\mathrm{Ga})}Z^{(^{69}\mathrm{Ga})}}. \quad (\mathrm{D1})$$

Substituting the standard constants in Eq. (D1) we find $E_{\mathrm{OHS}}^{(^{27}\mathrm{Al})}/E_{\mathrm{OHS}}^{(^{69}\mathrm{Ga})} \approx 1.18\rho^{\mathrm{Al}}/\rho^{\mathrm{Ga}}$. With the measured $E_{\mathrm{OHS}}^{(^{69}\mathrm{Ga})} \approx 21$ μeV (Fig. 9), the expected ^{27}Al Overhauser shift is $E_{\mathrm{OHS}}^{(^{27}\mathrm{Al})} \approx 4$ μeV ($E_{\mathrm{OHS}}^{(^{27}\mathrm{Al})} \approx 6$ μeV) for QDs type A (QDs type B), i.e., well above the minimum detectable levels.

Our explanation to this experimentally observed discrepancy is that ^{27}Al nuclei are polarized less efficiently than other isotopes (resulting in reduced σ_N of aluminium). A possible reason for reduced DNP efficiency of ^{27}Al is the smaller values of the envelope wave-function density in the barrier resulting in weaker hyperfine interaction between the electron and each individual nucleus. The ^{27}Al nuclear spin polarization can then be reduced further by fast spin diffusion in the barriers as opposed to the slow diffusion at the dot-barrier interface [45] stabilizing the polarization of As and Ga isotopes within the dot. These observations also suggest that the small values of the electron g factors are most likely due to the wave function penetrating into the AlGaAs barriers rather than due to diffusion of Al into the QD GaAs layer during the growth.

[1] B. Urbaszek, X. Marie, T. Amand, O. Krebs, P. Voisin, P. Maletinsky, A. Hoegele, and A. Imamoglu, Rev. Mod. Phys. **85**, 79 (2013).

[2] O. Gywat, H. J. Krenner, and J. Berezovsky, *Spins in Optically Active Quantum Dots*, 1st ed. (Wiley-VCH, Weinheim, 2010).

[3] D. Press, K. De Greve, P. L. McMahon, T. D. Ladd, B. Friess, C. Schneider, M. Kamp, S. Höfling, A. Forchel, and Y. Yamamoto, Nat. Photonics **4**, 367 (2010).

[4] K. De Greve, P. L. McMahon, D. Press, T. D. Ladd, D. Bisping, C. Schneider, M. Kamp, L. Worschech, S. Höfling, A. Forchel, and Y. Yamamoto, Nat. Phys. **7**, 872 (2011).

[5] T. M. Godden, J. H. Quilter, A. J. Ramsay, Y. Wu, P. Brereton, S. J. Boyle, I. J. Luxmoore, J. Puebla-Nunez, A. M. Fox, and M. S. Skolnick, Phys. Rev. Lett. **108**, 017402 (2012).

[6] A. V. Khaetskii, D. Loss, and L. Glazman, Phys. Rev. Lett. **88**, 186802 (2002).

[7] I. A. Merkulov, A. L. Efros, and M. Rosen, Phys. Rev. B **65**, 205309 (2002).

[8] E. A. Chekhovich, M. N. Makhonin, A. I. Tartakovskii, A. Yacoby, H. Bluhm, K. C. Nowack, and L. M. K. Vandersypen, Nat. Mater. **12**, 494 (2013).

[9] W. A. Coish and D. Loss, Phys. Rev. B **70**, 195340 (2004).

[10] A. S. Bracker, E. A. Stinaff, D. Gammon, M. E. Ware, J. G. Tischler, A. Shabaev, A. L. Efros, D. Park, D. Gershoni, V. L. Korenev, and I. A. Merkulov, Phys. Rev. Lett. **94**, 047402 (2005).

[11] B. Urbaszek, P.-F. Braun, T. Amand, O. Krebs, T. Belhadj, A. Lemaître, P. Voisin, and X. Marie, Phys. Rev. B **76**, 201301 (2007).

[12] D. J. Reilly, J. M. Taylor, J. R. Petta, C. M. Marcus, M. P. Hanson, and A. C. Gossard, Science **321**, 817 (2008).

[13] M. Issler, E. M. Kessler, G. Giedke, S. Yelin, I. Cirac, M. D. Lukin, and A. Imamoglu, Phys. Rev. Lett. **105**, 267202 (2010).

[14] A. Bechtold, D. Rauch, F. Li, T. Simmet, P.-L. Ardelt, A. Regler, K. Muller, N. A. Sinitsyn, and J. J. Finley, Nat. Phys. **11**, 1005 (2015).

[15] R. Stockill, C. Le Gall, C. Matthiesen, L. Huthmacher, E. Clarke, M. Hugues, and M. Atature, arXiv:1512.01811.

[16] Y. Kato, R. C. Myers, D. C. Driscoll, A. C. Gossard, J. Levy, and D. D. Awschalom, Science **299**, 1201 (2003).

[17] J. Pingenot, C. E. Pryor, and M. E. Flatté, Appl. Phys. Lett. **92**, 222502 (2008).

[18] J. Pingenot, C. E. Pryor, and M. E. Flatté, Phys. Rev. B **84**, 195403 (2011).

[19] T. Belhadj, T. Kuroda, C.-M. Simon, T. Amand, T. Mano, K. Sakoda, N. Koguchi, X. Marie, and B. Urbaszek, Phys. Rev. B **78**, 205325 (2008).

[20] M. Abbarchi, T. Kuroda, T. Mano, K. Sakoda, and M. Gurioli, Phys. Rev. B **81**, 035334 (2010).

[21] G. Sallen, S. Kunz, T. Amand, L. Bouet, T. Kuroda, T. Mano, D. Paget, O. Krebs, X. Marie, K. Sakoda, and B. Urbaszek, Nat. Commun. **5**, 3268 (2014).

[22] P. Atkinson, E. Zallo, and O. G. Schmidt, J. Appl. Phys. **112**, 054303 (2012).

[23] Y. H. Huo, A. Rastelli, and O. G. Schmidt, Appl. Phys. Lett. **102**, 152105 (2013).

[24] W. B. Gao, A. Imamoglu, H. Bernien, and R. Hanson, Nat. Photonics **9**, 363 (2015).

[25] N. Akopian, L. Wang, A. Rastelli, O. G. Schmidt, and V. Zwiller, Nat. Photonics **5**, 230 (2011).

[26] J.-P. Jahn, M. Munsch, L. Béguin, A. V. Kuhlmann, M. Renggli, Y. Huo, F. Ding, R. Trotta, M. Reindl, O. G. Schmidt, A. Rastelli, P. Treutlein, and R. J. Warburton, Phys. Rev. B **92**, 245439 (2015).

[27] E. Chekhovich, K. Kavokin, J. Puebla, A. Krysa, M. Hopkinson, A. Andreev, A. Sanchez, R. Beanland, M. Skolnick, and A. Tartakovskii, Nat. Nanotechnol. **7**, 646 (2012).

[28] M. Bayer, G. Ortner, O. Stern, A. Kuther, A. A. Gorbunov, A. Forchel, P. Hawrylak, S. Fafard, K. Hinzer, T. L. Reinecke, S. N. Walck, J. P. Reithmaier, F. Klopf, and F. Schäfer, Phys. Rev. B **65**, 195315 (2002).

[29] J. Puebla, E. A. Chekhovich, M. Hopkinson, P. Senellart, A. Lemaître, M. S. Skolnick, and A. I. Tartakovskii, Phys. Rev. B **88**, 045306 (2013).

[30] E. A. Chekhovich, M. N. Makhonin, J. Skiba-Szymanska, A. B. Krysa, V. D. Kulakovskii, M. S. Skolnick, and A. I. Tartakovskii, Phys. Rev. B **81**, 245308 (2010).

[31] D. Gammon, S. W. Brown, E. S. Snow, T. A. Kennedy, D. S. Katzer, and D. Park, Science **277**, 85 (1997).

[32] K. L. Janssens, F. M. Peeters, and V. A. Schweigert, Phys. Rev. B **63**, 205311 (2001).

[33] T. Mano, M. Abbarchi, T. Kuroda, B. McSkimming, A. Ohtake, K. Mitsuishi, and K. Sakoda, Appl. Phys. Express **3**, 065203 (2010).

[34] C. E. Pryor and M. E. Flatté, Phys. Rev. Lett. **96**, 026804 (2006).

[35] E. L. Ivchenko and A. A. Kiselev, Fiz. Tekh. Poluprovodn. **26**, 1471 (1992) [Sov. Phys. Semicond. **26**, 827 (1992)].

[36] M. J. Snelling, E. Blackwood, C. J. McDonagh, R. T. Harley, and C. T. B. Foxon, Phys. Rev. B **45**, 3922 (1992).

[37] R. M. Hannak, M. Oestreich, A. P. Heberle, W. W. Rühle, and K. Köhler, Solid State Commun. **93**, 313 (1995).

[38] J. R. Mejía-Salazar, N. Porras-Montenegro, and L. E. Oliveira, J. Phys.: Condens. Matter **21**, 455302 (2009).

[39] A. Malinowski and R. T. Harley, Phys. Rev. B **62**, 2051 (2000).

[40] I. A. Yugova, A. Greilich, D. R. Yakovlev, A. A. Kiselev, M. Bayer, V. V. Petrov, Y. K. Dolgikh, D. Reuter, and A. D. Wieck, Phys. Rev. B **75**, 245302 (2007).

[41] V. Jovanov, T. Eissfeller, S. Kapfinger, E. C. Clark, F. Klotz, M. Bichler, J. G. Keizer, P. M. Koenraad, G. Abstreiter, and J. J. Finley, Phys. Rev. B **83**, 161303 (2011).

[42] A. J. Bennett, M. A. Pooley, Y. Cao, N. Skoeld, I. Farrer, D. A. Ritchie, and A. J. Shields, Nat. Commun. **4**, 1522 (2013).

[43] E. A. Checkhovich, M. M. Glazov, A. B. Krysa, M. Hopkinson, P. Senellart, A. Lemaître, M. S. Skolnick, and A. I. Tartakovskii, Nat. Phys. **9**, 74 (2013).

[44] W. A. Coish and J. Baugh, Phys. Status Solidi B **246**, 2203 (2009).

[45] A. E. Nikolaenko, E. A. Chekhovich, M. N. Makhonin, I. W. Drouzas, A. B. Van'kov, J. Skiba-Szymanska, M. S. Skolnick, P. Senellart, D. Martrou, A. Lemaître, and A. I. Tartakovskii, Phys. Rev. B **79**, 081303 (2009).

[46] C. W. Lai, P. Maletinsky, A. Badolato, and A. Imamoglu, Phys. Rev. Lett. **96**, 167403 (2006).

[47] C. Latta, A. Högele, Y. Zhao, A. N. Vamivakas, M. Maletinsky, M. Kroner, J. Dreiser, I. Carusotto, A. Badolato, D. Schuh, W. Wegscheider, M. Atatture, and A. Imamoglu, Nat. Phys. **5**, 758 (2009).

[48] We note that the PL peaks of QD B2 in Fig. 3(d) are red-shifted by 150 μeV from the corresponding PLE and DNP peaks in Figs. 3(e) and 3(f). This could be explained by a Coulomb shift [68]: In PLE experiments, ground-state exciton emission of QD A2 is measured, under these conditions photon absorption in QD B2 takes place while QD A2 is empty. By contrast, the PL from QD B2 is most likely observed when tunneling into QD A2 is blocked by an exciton already occupying QD A2; this exciton is then also responsible for shifting the ground-state energy of QD B2.

[49] E. A. Chekhovich, M. N. Makhonin, K. V. Kavokin, A. B. Krysa, M. S. Skolnick, and A. I. Tartakovskii, Phys. Rev. Lett. **104**, 066804 (2010).

[50] E. A. Chekhovich, A. B. Krysa, M. S. Skolnick, and A. I. Tartakovskii, Phys. Rev. B **83**, 125318 (2011).

[51] E. A. Chekhovich, M. Hopkinson, M. S. Skolnick, and A. I. Tartakovskii, Nat. Commun. **6**, 6348 (2015).

[52] M. Munsch, G. Wust, A. V. Kuhlmann, F. Xue, A. Ludwig, D. Reuter, A. D. Wieck, M. Poggio, and R. J. Warburton, Nat. Nanotechnol. **9**, 671 (2014).

[53] R. K. Sundfors, Phys. Rev. B **10**, 4244 (1974).

[54] G. S. Pearson and D. A. Faux, J. Appl. Phys. **88**, 730 (2000).

[55] M. Grundmann, O. Stier, and D. Bimberg, Phys. Rev. B **52**, 11969 (1995).

[56] C. Latta, A. Srivastava, and A. Imamoglu, Phys. Rev. Lett. **107**, 167401 (2011).

[57] A. Greilich, A. Shabaev, D. R. Yakovlev, A. L. Efros, I. A. Yugova, D. Reuter, A. D. Wieck, and M. Bayer, Science **317**, 1896 (2007).

[58] P. Maletinsky, M. Kroner, and A. Imamoglu, Nat. Phys. **5**, 407 (2009).

[59] M. N. Makhonin, E. A. Chekhovich, P. Senellart, A. Lemaître, M. S. Skolnick, and A. I. Tartakovskii, Phys. Rev. B **82**, 161309 (2010).

[60] M. Bayer, O. Stern, A. Kuther, and A. Forchel, Phys. Rev. B **61**, 7273 (2000).

[61] V. Jovanov, T. Eissfeller, S. Kapfinger, E. C. Clark, F. Klotz, M. Bichler, J. G. Keizer, P. M. Koenraad, M. S. Brandt, G. Abstreiter, and J. J. Finley, Phys. Rev. B **85**, 165433 (2012).

[62] P. Maletinsky, A. Badolato, and A. Imamoglu, Phys. Rev. Lett. **99**, 056804 (2007).

[63] P. Maletinsky, C. W. Lai, A. Badolato, and A. Imamoglu, Phys. Rev. B **75**, 035409 (2007).

[64] D. Gammon, A. L. Efros, T. A. Kennedy, M. Rosen, D. S. Katzer, D. Park, S. W. Brown, V. L. Korenev, and I. A. Merkulov, Phys. Rev. Lett. **86**, 5176 (2001).

[65] A. White, I. Hinchliffe, P. Dean, and P. Greene, Solid State Commun. **10**, 497 (1972).

[66] C. Weisbuch and C. Hermann, Phys. Rev. B **15**, 816 (1977).

[67] D. J. Chadi, A. H. Clark, and R. D. Burnham, Phys. Rev. B **13**, 4466 (1976).

[68] C. A. Kessler, M. Reischle, R. Robach, E. Koroknay, M. Jetter, H. Schweizer, and P. Michler, Phys. Status Solidi B **249**, 747 (2012).